photonics

MDPI

Article

Joint Modulation Format Identification and OSNR Monitoring Based on Amplitude-Analytic Complex Planes for Digital Coherent Receivers

Ruyue Xiao [1], Ming Hao [1,2,3,*], Shuang Liang [1], Weigang Hou [3,4] and Jianming Tang [5]

[1] School of Automation and Information Engineering, Sichuan University of Science and Engineering, Yibin 644000, China; 323085404114@stu.suse.edu.cn (R.X.); 323085404106@stu.suse.edu.cn (S.L.)
[2] Intelligent Perception and Control Key Laboratory of Sichuan Province, Yibin 644000, China
[3] School of Communications and Information Engineering, Chongqing University of Posts and Telecommunications, Chongqing 400065, China; houwg@cqupt.edu.cn
[4] Institute of Intelligent Communications and Network Security, Chongqing University of Posts and Telecommunications, Chongqing 400065, China
[5] The DSP Centre of Excellence, School of Computer Science and Electronic Engineering, Bangor University, Bangor LL57 1UT, UK; j.tang@bangor.ac.uk
* Correspondence: haoming@suse.edu.cn

Abstract

Joint modulation format identification (MFI) and optical signal-to-noise ratio (OSNR) monitoring constitutes one of the most critical functions integrated in digital coherent receivers, ensuring high flexibility and stability in elastic optical networks (EONs). Since signal amplitude information captures inherent characteristics associated with modulation formats and fluctuations induced by OSNR variations, a simple and effective optical performance monitoring (OPM) scheme based on an amplitude-analytic complex plane is proposed. By employing a multi-task learning algorithm incorporating the multi-order gated aggregation (MOGA) module, the proposed scheme enables simultaneous MFI and OSNR monitoring for polarization division multiplexed (PDM)-QPSK/-16QAM/-32QAM/-64QAM/-128QAM signals. The performance of the proposed scheme is numerically verified in 28 GBaud coherent optical communication systems of various configurations. Numerical simulation results show that 100% identification accuracy is obtainable for all five modulation formats, even at OSNR values lower than the corresponding theoretical 20% forward error correction (FEC) limit. Meanwhile, the mean absolute error (MAE) of OSNR monitoring for QPSK, 16QAM, 32QAM, 64QAM, and 128QAM are 0.16 dB, 0.15 dB, 0.17 dB, 0.28 dB, and 0.33 dB, respectively. Furthermore, simulation results show that the proposed scheme is robust to residual chromatic dispersion (CD) and the nonlinear effects with strong generalization capability. These results suggest that the proposed scheme is promising for applications in next-generation EONs.

Keywords: modulation format identification; OSNR monitoring; amplitude-analytic complex plane; multi-task learning network incorporating MOGA module; digital coherent receivers

Check for updates

Received: 28 March 2026
Revised: 19 April 2026
Accepted: 22 April 2026
Published: 24 April 2026

Copyright: © 2026 by the authors. Licensee MDPI, Basel, Switzerland. This article is an open access article distributed under the terms and conditions of the Creative Commons Attribution (CC BY) license.

1. Introduction

The rapid evolution of emerging technologies such as the mobile internet, big data and cloud computing has imposed unprecedented challenges on optical networks. Consequently, optical networks are evolving from predefined fixed operations toward flexible

and elastic solutions to meet the dynamic and heterogeneous demands of data traffic. The EONs [1] can dynamically adjust their transmission parameters, including, for example, bandwidth allocation, modulation format, baud rate, and signal power at the transmitters according to real-time traffic requirements and channel characteristics, thereby improving spectral efficiency and network operation flexibility [2]. Accordingly, at the digital coherent receivers, MFI [3–12] is essential to achieve self-adaptability and ultra-low latency. Meanwhile, since linear impairments of the transmitted signals can be nearly fully compensated at the digital coherent receivers, OSNRs serve as a critical metric for the transmission links. Therefore, OSNR monitoring [13–17] at receivers is also indispensable for guaranteeing the stability and flexibility of the EONs.

Generally speaking, monitoring techniques of digital coherent receivers can be categorized into multi-task model-based and single-task cascade model-based. Recently, benefiting from the powerful feature extraction and analysis capabilities of machine learning methods, it has become feasible to simultaneously identify subtle feature differences among diverse modulation formats and different OSNR values. Compared with single-task cascade model-based techniques, multi-task OPM enables feature sharing, avoids redundant computations, and allows rapid and comprehensive monitoring of these parameters [18]. The mainstream machine learning-based multitask OPM techniques utilize convolutional neural network (CNN) [19–29], binary neural network (BNN) [30], artificial neural network (ANN) [31–33], deep neural network (DNN) [34–37], long short-term memory (LSTM) [38], ternary neural network (TNN) [39], residual network (ResNet) [40–42], deep transfer learning (DTL) [43–45], random forest (RF) [46], and multi-model fitting network (MMFN) [47], as well as multi-feature fusion network (MFF-Net) [48]. However, all the aforementioned schemes are only applicable to signal monitoring with modulation formats up to 64QAM. In practice, the higher the modulation format order, the more challenging the signal monitoring becomes, particularly for OSNR monitoring. To address this challenge, several advanced schemes have been proposed to realize multi-task OPM for modulation formats up to 128QAM. These schemes include residual networks with attention mechanisms (SA-ResNet) [49], multi-task metric learning (MML) [50], multi-task model-agnostic meta-learning (MT-MAML) [51] and adaptive few-shot transfer learning networks (AFTLN) [52].

In this paper, a multi-task OPM scheme based on an amplitude-analytic complex plane is proposed by adopting the discrete Hilbert transform to construct an amplitude-analytic complex plane, which effectively enhances the separability of high-order modulated signals under severe noise conditions. Following feature extraction, a lightweight multi-task learning network incorporating a MOGA module is employed to realize joint MFI and OSNR monitoring synchronously. To validate the feasibility and effectiveness of the proposed scheme, numerical simulations are performed of 28 GBaud PDM-QPSK/-16QAM/-32QAM/-64QAM/-128QAM signals. The simulation results show that the proposed scheme enables high accuracy of MFI and OSNR monitoring for all the aforementioned modulation formats. Notably, for PDM-64QAM and PDM-128QAM signals, the accuracy of MFI remains at 100%, while the OSNR estimation error is maintained at a low level. Furthermore, the proposed scheme also exhibits favorable robustness against residual CD and fiber nonlinearity. These results suggest that the proposed scheme is a promising candidate for high-order modulated signal monitoring (up to 128QAM) for diverse practical optical communication scenarios.

2. Operating Principle

As illustrated in Figure 1, a representative digital signal processing (DSP) chain for a digital coherent receiver consists of three modules: modulation-format-independent

algorithms, the proposed multi-task OPM scheme, and modulation-format-dependent algorithms. The received digital signals are processed by using modulation-format-independent algorithms to compensate for CD impairments, timing jitter and polarization-related interferences. The proposed scheme is applied to identify the modulation format and estimate the OSNR. Based on the recognized modulation format, further polarization demultiplexing for mQAM ($m > 4$) signals can be implemented via the multi-modulus algorithm (MMA). Meanwhile, appropriate algorithms are selected to accomplish frequency offset compensation and carrier phase recovery. Additionally, the estimated OSNR can also be used for signal quality evaluation and provide feedback to the EON operation.

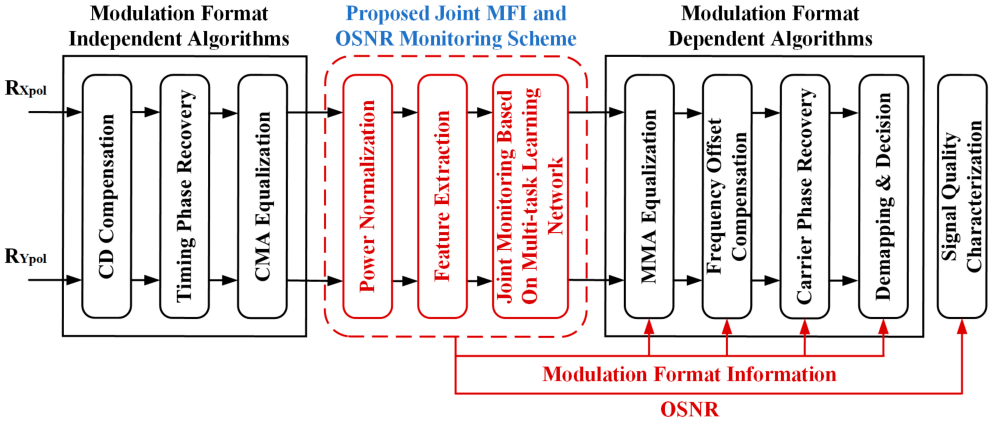


Figure 1. The DSP chain with the proposed joint monitoring scheme for digital coherent receivers.

As highlighted in the red box of Figure 1, the proposed scheme involves three sequential operations: Power normalization is firstly applied to the signals equalized by the constant modulus algorithm (CMA), followed by the construction of an amplitude-analytic complex plane. The extracted image features are then fed into a multi-task learning network incorporating a MOGA module to realize joint MFI and OSNR monitoring simultaneously.

2.1. Amplitude-Analytic Complex Plane

Since the phase information of a signal is severely degraded by phase noise, while carrier phase recovery is located at the final stage of the DSP chain and requires prior knowledge of the modulation format, the OPM has to rely on amplitude information for feature extraction. However, linear and nonlinear impairments along the transmission link distort the signal amplitude distribution, particularly for high-order modulation formats such as 64QAM and 128QAM. Consequently, it is challenging to achieve accurate multi-task OPM for high-order modulation formats by using one-dimensional amplitude information only.

The discrete Hilbert transform (DHT) applied to the signal amplitude enables effective extraction of amplitude fluctuation features. As different modulation formats exhibit distinct amplitude fluctuation characteristics, the DHT can transform these subtle variations into learnable features, thereby facilitating the accurate extraction of the instantaneous signal characteristics.

Assume that the amplitude of received signals, $X[n]$, is a real-valued sequence with length N, where $n = 0, 1, \cdots, N-1$, and N is the number of symbols.

Firstly, the discrete Fourier transform (DFT) is applied to the signal amplitude sequence to convert it into the frequency domain. The process can be expressed as:

$$X[k] = \sum_{n=0}^{N-1} X[n]_e^{-j\frac{2\pi}{N}kn}, k = 0, 1, \cdots, N-1 \quad (1)$$

where $X[k]$ denotes the frequency-domain signal, and k is the frequency tone.

Then, $X[k]$ is processed in the frequency domain, and the calculated signal $H[k]$ is given as:

$$H[k] = \begin{cases} -jX[k], 1 \le k \le \frac{N}{2} - 1 \\ jX[k], \frac{N}{2} + 1 \le k \le N - 1 \\ X[k], k = 0, \frac{N}{2} \end{cases} \quad (2)$$

Finally, the calculated frequency-domain signal $H[k]$ is transformed back to the time domain via the inverse discrete Fourier transform (IDFT), and the signal after IDFT can be defined as:

$$\hat{X}[n] = \frac{1}{N} \sum_{k=0}^{N-1} H[k]_e^{j\frac{2\pi}{N}kn}, n = 0, 1, \cdots, N-1 \quad (3)$$

By applying DHT, $X[n]$ has been transformed into $\hat{X}[n]$. Then, the amplitude-analytic complex plane can be constructed. In the amplitude-analytic complex plane, the horizontal axis is $X[n]$, and the vertical axis is $\hat{X}[n]$. Therefore, the amplitude-analytic complex plane not only characterizes the amplitude distribution of different modulation formats but also captures their amplitude fluctuation features. Since the amplitude fluctuation differs distinctly across modulation formats and also varies with OSNR, as shown in Figure 2, they form distinguishable clustering distributions on the amplitude-analytic complex plane.

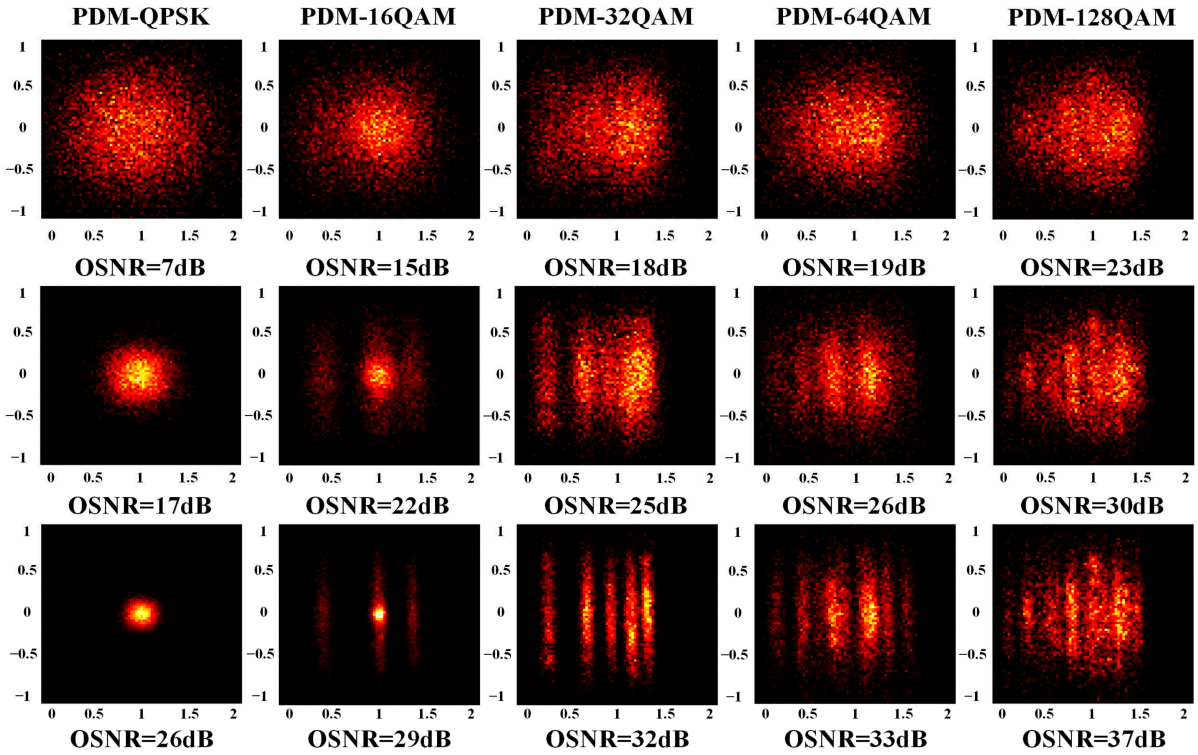


Figure 2. The amplitude-analytic complex planes for PDM-QPSK/-16QAM/-32QAM/-64QAM/-128QAM with different OSNR values.

The position of each symbol on the amplitude-analytic complex plane is determined by its amplitude and the DHT of amplitude. With a fixed number of symbols, their grid distribution is determined by both the modulation format and the value of OSNR. The QPSK, 16QAM, 32QAM, 64QAM and 128QAM signals possess 1, 3, 5, 9 and 13 amplitude levels, respectively, which can be clearly observed in the amplitude-analytic complex planes at high OSNR values. In low OSNR cases, such distinct distribution features are

obscured. Nevertheless, benefiting from the DHT of the signal amplitude, as illustrated in Figure 2, different modulation formats still retain their distinguishable characteristics in the amplitude-analytic complex plane even under low OSNR conditions.

2.2. Multi-Task Learning Network Incorporating a MOGA Module

As mentioned above, both MFI and OSNR monitoring are derived from the features in the amplitude-analytic complex plane. During optical fiber transmissions, the signal characteristics degrade under linear and nonlinear impairments, leading to a gradual reduction in the discrepancy between fine-grained features and global statistical features. As the network coverage increases, low-level discriminative information may be lost during feature propagation, thereby affecting the performance of multi-parameter joint prediction. Therefore, it is necessary to develop a multi-task collaborative modeling architecture that can strengthen multi-scale representation while still maintaining stable information transmission. Accordingly, a lightweight multi-task learning network embedded with the MOGA module is proposed to realize the joint MFI and OSNR monitoring.

As shown in Figure 3, the amplitude-analytic complex plane is applied as the input feature to the proposed multi-task learning network, and sequentially passes through a convolutional layer, a batch normalization layer, a ReLU activation function, and a max pool layer to complete the basic feature extraction, and then performs deep feature modeling by the MOGA module. This module consists of four stages: feature decomposition, multi-order spatial modeling, gated modulation and residual fusion. Firstly, in the feature decomposition stage, as shown in Figure 3b, linear projection is performed via 1×1 convolution, and a global statistical vector is extracted by using global average pooling (GAP). Subsequently, a learnable scaling factor $\boldsymbol{r}$ is applied to adaptively recalibrate the difference between the input feature and its global mean, thereby enhancing the contrast between the local fine-grained textures and global structures, which can be regarded as constructing a learnable high-frequency enhancement mechanism. In the multi-order spatial modeling stage, the numerical branch is constructed, as shown in the dashed box on the right of Figure 3c. Multi-scale modeling is achieved via depthwise separable convolutions with different dilation rates: DWConv5 $\times$ 5 (d = 1) characterizes low-order local neighborhood information, DWConv5 $\times$ 5 (d = 2) and DWConv7 $\times$ 7 (d = 3) capture mid-order and high-order global information, respectively. After the concatenation along the channel dimension, the features are fused via 1×1 pointwise convolution and activated by SiLU to form the multi-order numerical feature $\mathbf{v}$ in the right branch of Figure 3c. Meanwhile, a gating branch is constructed, as shown in the left branch of Figure 3c. The gating weight $\mathbf{g}$ is generated by a 1×1 convolution, activated with SiLU, and then multiplied element-wise with the multi-order numerical feature $\mathbf{v}$ to achieve adaptive feature selection and dynamic modulation. Subsequently, the features are compressed via 1×1 convolution to generate new features. Then the original input features are added to the gated aggregation result through an identity mapping path to complete residual fusion. Finally, the fused features undergo channel fusion and distribution stabilization via the convolutional layer, the batch normalization layer, and the ReLU activation function. They are then converted into compact statistical vectors through GAP to provide discriminative feature representations for MFI and OSNR monitoring. This structure, based on multi-order modeling, gated modulation and residual stabilization, ensures stable gradient propagation while achieving adaptive enhancement of multi-scale features, thus guaranteeing reliable and high-precision recognition performance.

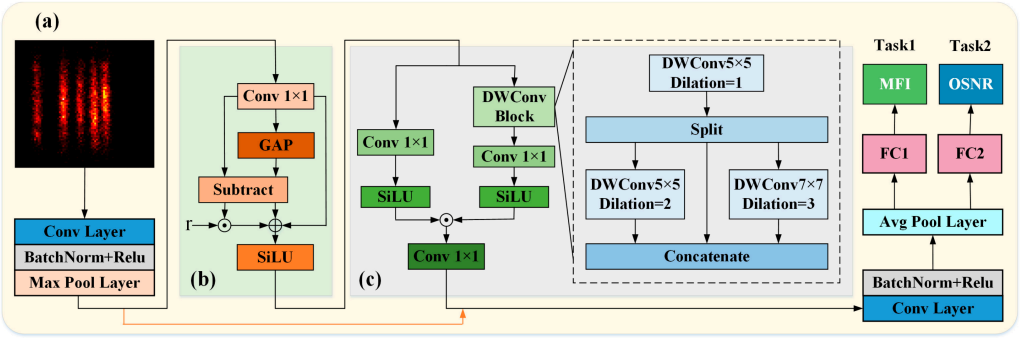


Figure 3. Schematic diagram of the multi-task learning network incorporating the MOGA module. (**a**) Overall architecture of the proposed multi-task learning network; (**b**) feature decomposition stage; (**c**) multi-order spatial modeling stage and gated modulation stage.

3. Numerical Simulation Results and Analysis

To verify the proposed scheme, a 28 GBaud PDM transmission system is established by using a *VPI Transmission Maker 11.1*, as shown in Figure 4. At the transmitter, an external cavity laser (ECL) generates an optical carrier at 1550 nm with a linewidth of 100 kHz. Then, this optical carrier is split by a polarization beam splitter (PBS) and modulated by two I/Q modulators. After a polarization beam combiner (PBC), the PDM signals are launched into three distinct transmission links. As illustrated in Figure 4, link (1) employs a back-to-back (BTB) configuration for performance analysis, link (2) incorporates CD to evaluate the dispersion tolerance of the proposed scheme, and link (3) utilizes long-haul fiber transmissions to verify both robustness against fiber nonlinear effects and the generalization capability of the proposed scheme. For link (3), the long-haul transmission link consists of $M \times 80$ km single-mode fiber (SMF) spans with $M = 25$ for QPSK, $M = 13$ for 16QAM, $M = 5$ for 32QAM, $M = 3$ for 64QAM, and $M = 2$ for 128QAM. The deployed SMF exhibits a CD parameter of $D = 16$ ps/nm/km, a polarization-mode dispersion parameter of $D_{PMD} = 0.1$ ps/km$^{1/2}$, an attenuation coefficient of $\alpha = 0.2$ dB/km, and a nonlinear coefficient of $\gamma = 1.267$ km^{-1}W^{-1}. An Erbium-doped fiber amplifier (EDFA) with a noise figure of 5 dB is utilized to compensate for the fiber loss in each span. At the receiver, the incoming optical signal is combined with a local oscillator (LO) in a polarization-diversity hybrid, followed by detection using a balanced photodetector. Subsequently, the sampled digital signals obtained by analog-to-digital converters (ADCs) are processed in an offline DSP module.

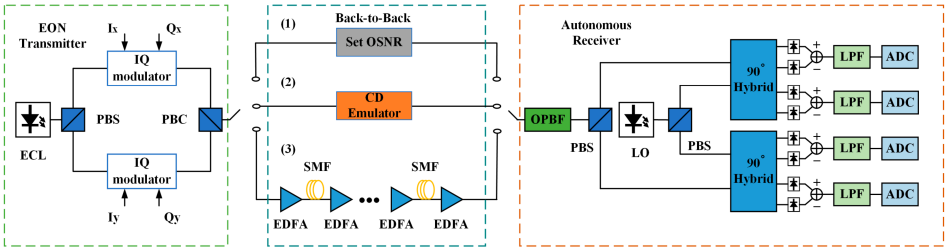


Figure 4. The simulation setup of the PDM coherent optical transmission system.

The performance of the proposed scheme is first verified in the BTB link. The OSNR ranges for the PDM-QPSK/-16QAM/-32QAM/-64QAM/-128QAM signals are 7–26 dB, 15–29 dB, 18–32 dB, 19–33 dB, and 23–37 dB, respectively, with a step size of 1 dB. In the BTB case, for each OSNR value corresponding to each modulation format, 100 independent samples are extracted, resulting in a dataset with 8000 samples. The dataset is further divided into a training set and a testing set in an 8:2 ratio for subsequent training and performance analysis.

The performance of the proposed scheme under different image dimensions and number of symbols is depicted in Figure 5. The image dimension affects the fine granularity of feature extraction, while the number of symbols determines the computational complexity and latency of the proposed scheme. These two factors collectively govern the overall monitoring performance. Figure 5a illustrates the accuracy of MFI under various image dimensions (28 × 28, 56 × 56, 112 × 112) and number of symbols (2000, 4000, 6000, 8000, 10,000). It can be observed that 100% correct identification rates are achieved under most parameter combinations, except that only one case (28 × 28, 2000 symbols) is slightly below 100%. The accuracy of MFI maintains its remarkable stability across various settings, which validates the superior robustness of the proposed scheme for performing MFI tasks. Figure 5b indicates the MAE of OSNR estimation under various settings. Unlike MFI, the OSNR estimation is a regression task and more sensitive to the number of symbols. The overall trend in Figure 5b is that the MAE of OSNR estimation decreases as the number of symbols increases. However, when the number of symbols is increased to 8000, the MAE is almost identical to that of the 10,000 symbols case. The impact of image dimension on MAE can be regarded as nearly negligible. Therefore, considering the computational complexity and latency, the image dimension and number of symbols are set at 28 × 28 and 8000, respectively.

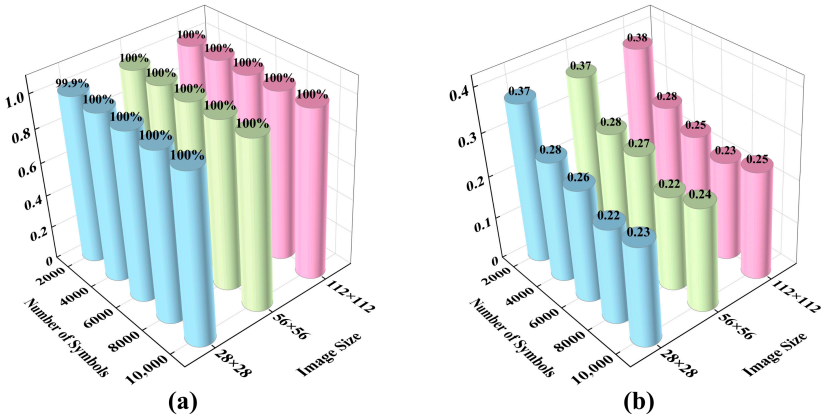


Figure 5. (**a**) The correct rate of MFI and (**b**) the MAE of OSNR estimation under different image dimensions and number of symbols.

Figure 6 shows the correct identification rates of the 28 GBaud PDM-QPSK/-16QAM/-32QAM/-64QAM/-128QAM signals under different OSNR values. In this figure, each dashed line with a color identical to the corresponding modulation format represents an OSNR threshold corresponding to a 20% FEC. It can be clearly seen that all five modulation formats can be identified with an accuracy of 100% over a wide OSNR range.

The OSNR monitoring performance of the proposed scheme is illustrated in Figure 7a–e, which corresponds to QPSK, 16QAM, 32QAM, 64QAM, and 128QAM, respectively. The horizontal axis represents the true OSNR values, the vertical axis denotes the estimated OSNR values, and the red scatter points correspond to the outputs of the proposed scheme. The estimated OSNR values are uniformly distributed in the vicinity of the dashed diagonal line, demonstrating that the proposed scheme possesses strong regression capability and high estimation accuracy. It should also be noted that as the modulation order increases, the estimation error increases slightly. This occurs because the amplitude levels of high-order modulation formats become more densely distributed, resulting in degraded anti-interference performance.

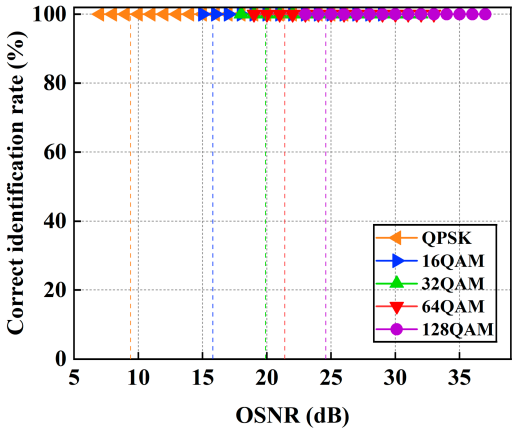


Figure 6. The correct MFI rates for the five modulation formats under different OSNR values.

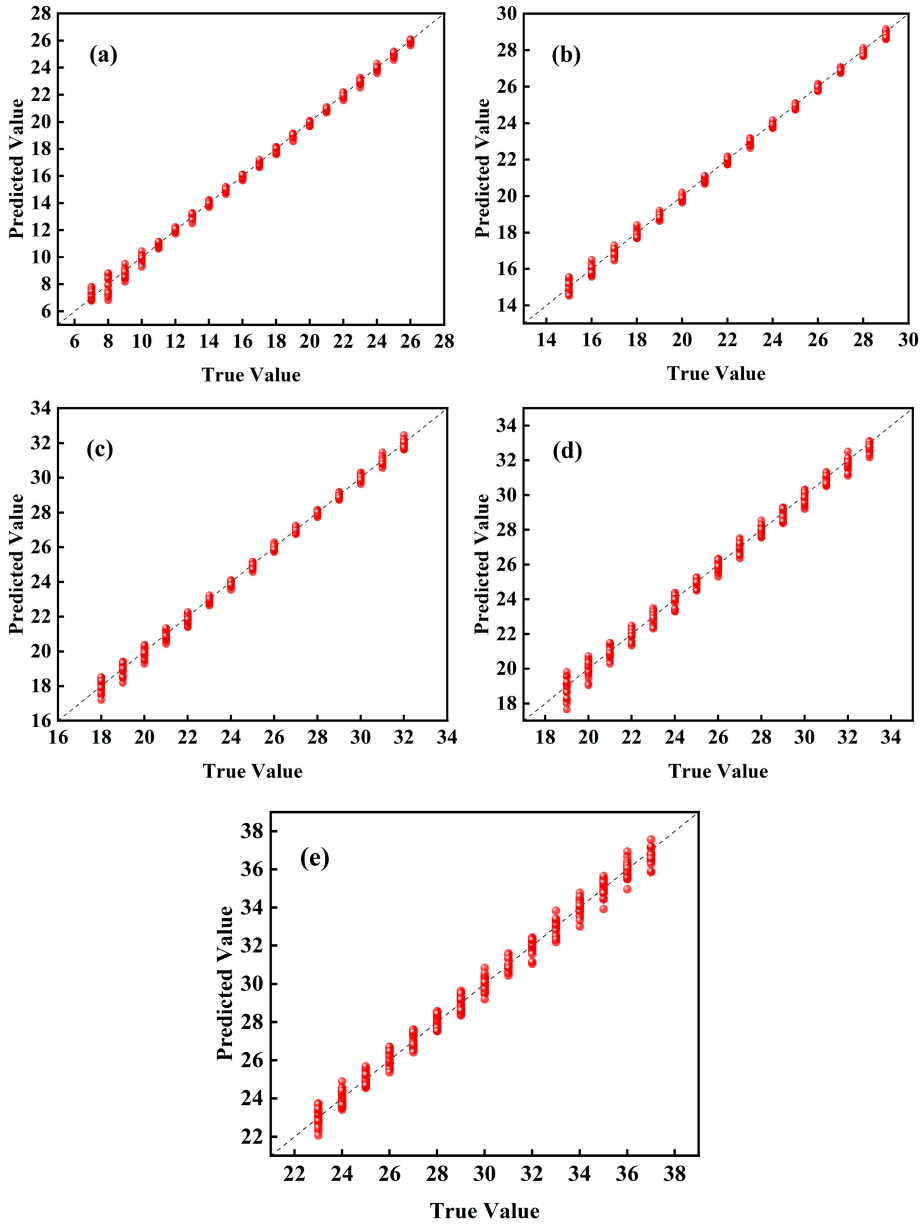


Figure 7. True OSNR values and estimated OSNR values for the five modulation formats: (**a**) QPSK, (**b**) 16QAM, (**c**) 32QAM, (**d**) 64QAM, and (**e**) 128QAM.

To further analyze the OSNR monitoring performance, the MAE of OSNR estimation is presented in Figure 8, where the dashed lines represent the overall MAE of the corresponding modulation formats, and the triangles denote the MAE at the specific OSNR values. The overall MAE values for QPSK, 16QAM, 32QAM, 64QAM, and 128QAM are 0.16 dB, 0.15 dB, 0.17 dB, 0.28 dB, and 0.33 dB, respectively. As shown in these five figures, except for the extremely low OSNR value in Figure 8a, the MAE of OSNR estimation is less than 0.5 dB for each specific OSNR. At extremely low OSNR values, strong noise causes severe fluctuation of the features, which increases the difficulty of estimation. On the other hand, in the high OSNR region, the feature discrimination between adjacent OSNR values decreases, resulting in a slight increase in the estimation error.

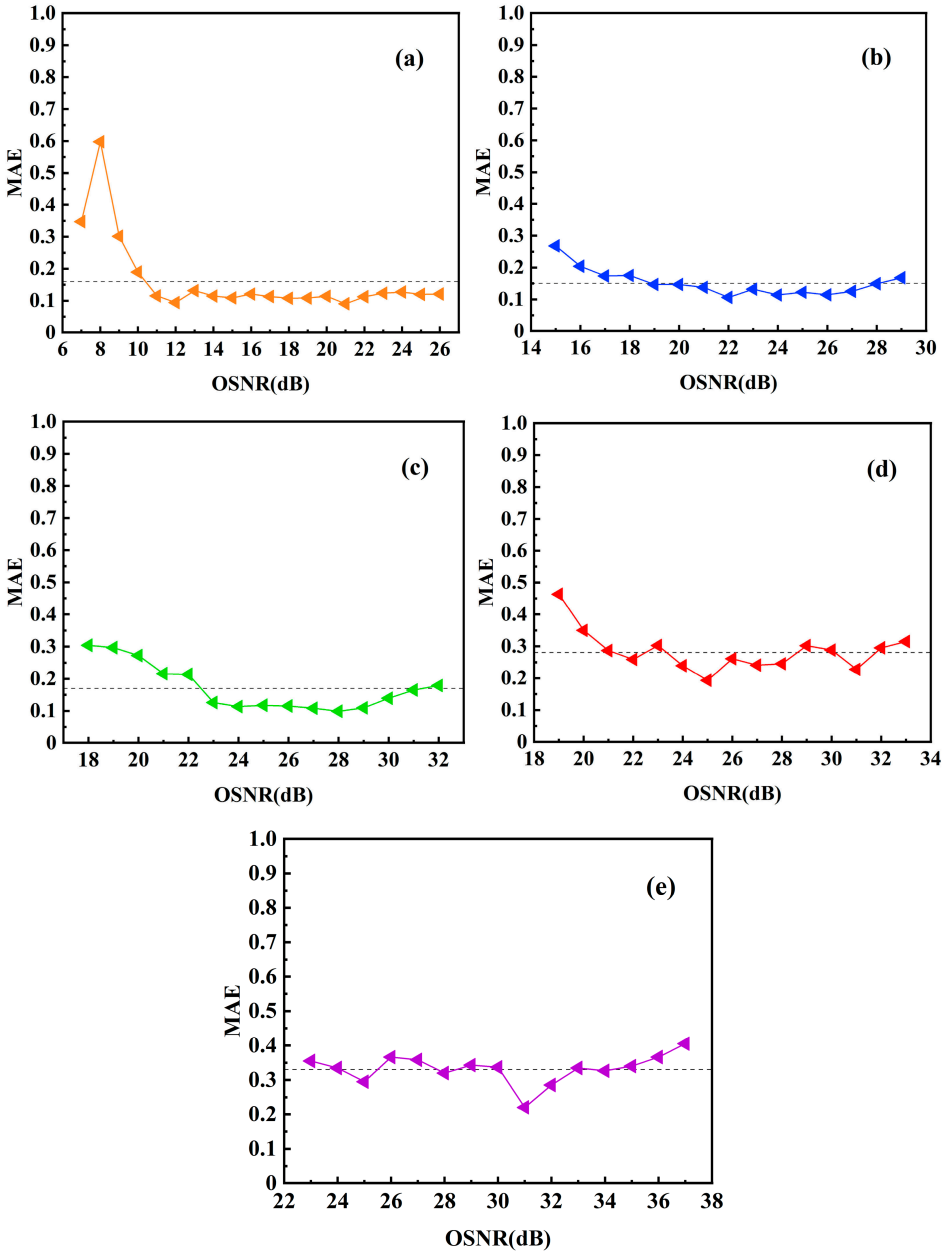


Figure 8. The MAE of OSNR estimation for (**a**) QPSK, (**b**) 16QAM, (**c**) 32QAM, (**d**) 64QAM, and (**e**) 128QAM under different OSNR values.

To analyze the robustness of the proposed scheme against frequency offset, a frequency offset of 100 MHz is set under BTB conditions. The correct MFI rates for the five modulation formats under a frequency offset of 100 MHz are shown in Figure 9a. 100% accuracy of MFI

is achieved over the entire OSNR range, even if the OSNR is lower than the corresponding theoretical 20% FEC limit. The MAE of OSNR estimation for the five modulation formats under a frequency offset of 100 MHz is illustrated in Figure 9b. The overall MAE for QPSK, 16QAM, 32QAM, 64QAM, and 128QAM are 0.21 dB, 0.19 dB, 0.26 dB, 0.37 dB, and 0.69 dB, respectively. Except for 128QAM, the MAE of other modulation formats does not increase noticeably. This is because 128QAM has significantly lower tolerance to frequency offset compared with other lower-order modulation formats, and the frequency offset results in severe feature degradation. Nevertheless, the degradation of OSNR estimation performance caused by frequency offset is within an acceptable range, demonstrating that the proposed scheme is robust against frequency offset.

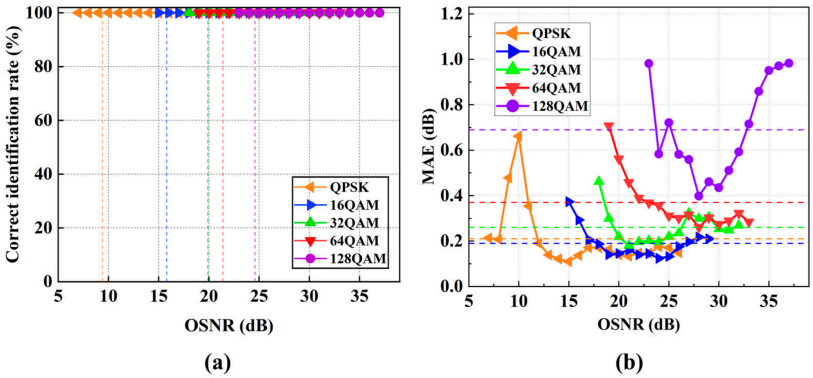


Figure 9. The (**a**) correct MFI rates and (**b**) MAE of OSNR estimation for the five modulation formats under a frequency offset of 100 MHz.

In the DSP module, the front-end CD compensation algorithm may still leave some residual dispersion after compensation. In order to further evaluate the influence of residual CD on the proposed scheme, link (2), as shown in Figure 4, is applied. The residual CD is set to a range from −90 ps/nm to 90 ps/nm with a step size of 30 ps/nm. The multi-task learning network trained in the BTB case is still applied under the current scenario, while for each OSNR value corresponding to each modulation format and each residual CD value, 20 independent samples are extracted to construct the test set. As shown in Figure 10, the MFI accuracy of the five modulation formats still remains at 100% even when the residual CD is increased to ±90 ps/nm. The residual CD can cause severe feature degradation, thereby increasing the error of OSNR estimation. The MAE of OSNR estimation generally exhibits an upward trend with the accumulation of residual CD. Nevertheless, the proposed scheme still demonstrates a certain tolerance to residual CD. Within the range of −60 ps/nm to 90 ps/nm, the MAE of OSNR estimation for all modulation formats is still less than 1 dB.

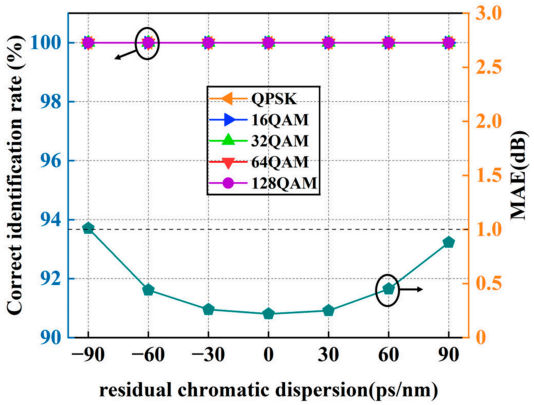


Figure 10. Correct MFI rate and MAE of OSNR estimation under different residual CD.

Nonlinear impairments tend to occur under long-haul transmissions or high launching powers, which can also lead to feature degradations. In order to evaluate the influence of the nonlinear effect on the proposed scheme, link (3), as shown in Figure 4, is applied. In the long-haul transmission case, the training set is generated by using samples obtained at a launching power of 0 dBm only. For each OSNR value corresponding to each modulation format, 80 independent samples are extracted. Meanwhile, for each OSNR value corresponding to each modulation format and each launching power, 20 independent samples are extracted to construct the test set. The transmission distances for QPSK, 16QAM, 32QAM, 64QAM, and 128QAM signals are 2000 km, 1040 km, 400 km, 240 km, and 160 km, respectively. The OSNR ranges for the five modulation formats are identical to those adopted in the BTB case. The launching power is set to vary from −3 dBm to 5 dBm. It can be seen from Figure 11 that even if the launching power is increased to 5 dBm, the accuracy of MFI for all five modulation formats still remains 100%. OSNR estimation is more significantly affected by the nonlinear effects. When the launching power is less than 2 dBm, the overall MAE of OSNR estimation can be kept below 1 dB. When the launching power exceeds 2 dBm, the influence of the nonlinear effects on the features becomes significant, leading to a substantial increase in MAE. One of the advantages of the proposed scheme is its strong generalization ability. The training set is established by only using data obtained at a launching power of 0 dBm, yet it can still maintain a high estimation accuracy when applied to test data under other launching powers. For the proposed scheme, changes in transmission scenarios and parameters do not require model retraining, which ensures the flexibility of the system.

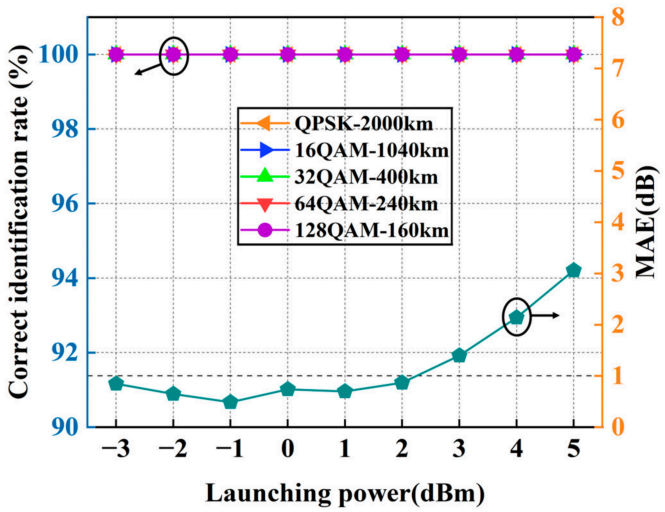


Figure 11. Correct MFI rate and MAE of OSNR estimation under different launching powers.

To further evaluate the validity of the amplitude-analytic complex plane, a comparative analysis of the schemes employing the amplitude-analytic complex plane, constellation diagram, and Stokes space feature is carried out under identical conditions and is shown in Figure 12. The constellation diagram is also based on the CMA-equalized signal, while the Stokes space feature is extracted from the S_1–S_3 plane. Both the constellation diagram and Stokes space feature are similarly fed into the multi-task learning network incorporating a MOGA module. As shown in Figure 12a, the overall correct MFI rates for the schemes employing the amplitude-analytic complex plane, constellation diagram, and Stokes space feature are 99.2%, 99.9%, and 100%, respectively. The constellation diagram based on the CMA-equalized signal is inevitably affected by phase noise, while high-order modulation formats lead to an excessive number of clusters in Stokes space, thus posing challenges to feature extraction. As illustrated in Figure 12b, the proposed scheme exhibits more distinct

advantages in OSNR estimation. The impact of feature extraction effectiveness on OSNR monitoring is more significant.

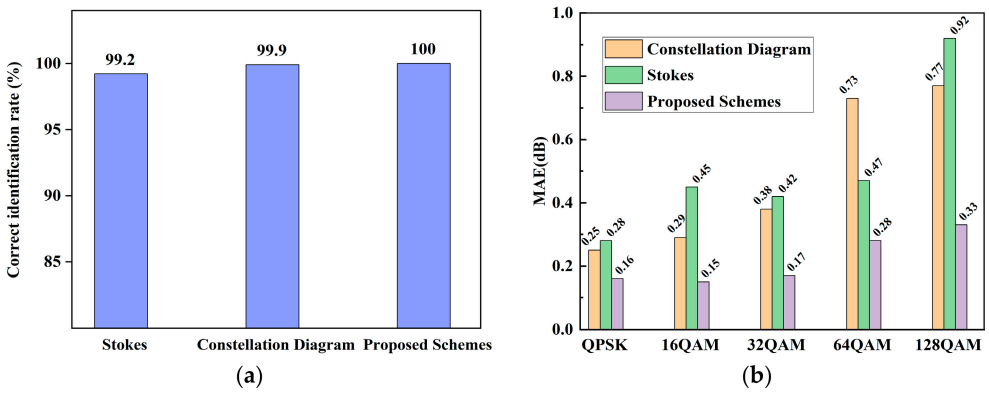


Figure 12. The overall (**a**) correct MFI rates and (**b**) MAE of OSNR estimation for the scheme employing the amplitude-analytic complex plane, constellation diagram, and Stokes space feature.

To further verify the advantages of the proposed scheme in terms of the trade-off between computational complexity and performance, comparisons are made between the proposed technique and typical deep learning network models, including DenseNet [53], ResNet [54], MobileNet [55], and VGG-like [56]. The relevant results are presented in Table 1 and Figure 13. Params and FLOPs are calculated by using THOP (Torch OpCounter). As a lightweight tool designed for PyTorch 2.3.1, THOP is adopted to compute the number of model parameters (Params) and computational cost (FLOPs) for evaluating model complexity. As seen in Table 1, the number of parameters of the proposed scheme is just 0.04 M, and its computational complexity is 112.41 M FLOPs. Compared with DenseNet, ResNet, MobileNet and VGG-like models, both the parameter scale and computational cost are significantly reduced, demonstrating excellent lightweight characteristics. The offline processing is conducted on a graphics workstation equipped with an Intel Core i9-13900K CPU running at 3 GHz, 128 GB of RAM, and an RTX A6000 graphics card with 48 GB of video memory. Under this hardware configuration, the total training time of the proposed scheme is 26.76 s, and the average execution time per test sample is 12.02 ms. As observed in Figure 13, all the schemes can achieve high accuracy (close to or reaching 100%) in the MFI task. In contrast, the performance differences among different schemes are more distinct in the OSNR estimation task. The proposed scheme achieves lower MAE under all modulation formats and maintains stable estimation accuracy even for high-order modulation formats such as 64QAM and 128QAM, demonstrating strong robustness. Based on the above results, the proposed scheme significantly reduces computational complexity while maintaining high performance. This effectively enhances the practicality and deployment potential of the proposed scheme.

Table 1. Comparison of computational complexity among five schemes.

Schemes	Params	FLOPs
DenseNet	38.39 M	18,635.71 M
ResNet	23.52 M	2559.24 M
MobileNet	3.51 M	238.31 M
VGG-like	4.27 M	212.07 M
Proposed Schemes	0.04 M	112.41 M

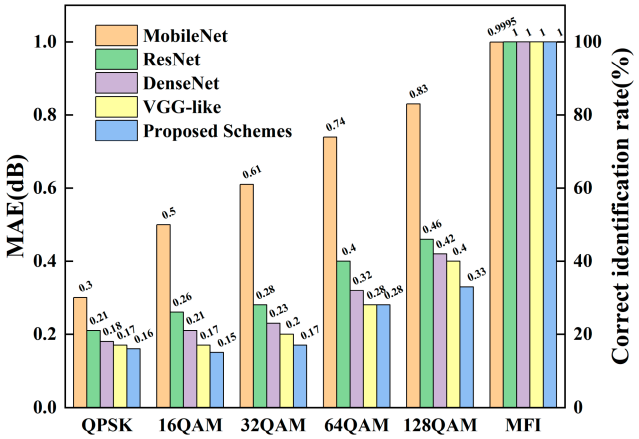


Figure 13. Correct MFI rate and MAE of OSNR estimation of five schemes.

4. Discussion

The proposed scheme is capable of supporting more modulation formats, including 8QAM. Even with the addition of 8QAM, all six modulation formats can be identified with 100% accuracy when the OSNR is lower than the corresponding theoretical 20% FEC limit. However, the MAE of OSNR estimation for 8QAM signals is higher than that for other higher-order modulation formats. This phenomenon arises because the features in the amplitude-analytic complex plane exhibit high similarity for 8QAM signals under different OSNR values, resulting in a relatively degraded regression performance. Nevertheless, the MAE value of 0.4 dB remains within an acceptable range for practical applications.

Actually, the proposed scheme only employs the CMA-equalized signal from one polarization for feature extraction and identification. Therefore, if the signals of the X-polarization and Y-polarization adopt different modulation formats (hybrid modulation formats), feature extraction can be performed separately on X-polarization and Y-polarization signals after CMA equalization.

5. Conclusions

In this paper, for digital coherent receivers, a joint MFI and OSNR monitoring scheme has been proposed, in which, based on the amplitude-analytic complex plane, a multi-task learning algorithm incorporating the MOGA module is developed to realize simultaneous MFI and OSNR monitoring for PDM-QPSK/-16QAM/-32QAM/-64QAM/-128QAM signals. The proposed scheme is numerically verified in a 28 GBaud coherent optical communication system of various configurations. Simulation results have demonstrated that the proposed scheme enables high accuracy of MFI and OSNR monitoring. In addition, it also exhibits strong robustness against residual CD and the nonlinear effects and has excellent generalization capability. Furthermore, compared with other relevant schemes, the proposed scheme achieves a lower MAE in OSNR estimation while maintaining lightweight characteristics. Therefore, the proposed scheme is promising for guaranteeing the stability and flexibility of next-generation EONs.

Author Contributions: Conceptualization, R.X. and M.H.; methodology, R.X. and M.H.; software, R.X. and S.L.; validation, R.X. and S.L.; formal analysis, R.X. and M.H.; writing—original draft preparation, M.H. and R.X.; writing—review and editing, J.T. and W.H.; supervision, M.H. and W.H.; project administration, M.H. and J.T.; funding acquisition, M.H. and J.T. All authors have read and agreed to the published version of the manuscript.

Funding: This research was partly supported by the North Wales Growth Deal through Ambition North Wales, partly supported by UK Research and Innovation (UKRI) Engineering and Phys-

ical Sciences Research Council (EPSRC) Projects, including TITAN [EP/Y037243/1] and HASC [EP/X040569/1], as well as partly supported by the Postgraduate Innovation Fund of Sichuan University of Science and Engineering (Y2024295).

Institutional Review Board Statement: Not applicable.

Informed Consent Statement: Not applicable.

Data Availability Statement: Data underlying the results presented in this paper are not publicly available at this time but may be obtained from the authors upon reasonable request.

Conflicts of Interest: The authors declare no conflicts of interest.

References

1. Tomkos, I.; Azodolmolky, S.; Sole-Pareta, J.; Careglio, D.; Palkopoulou, E. A tutorial on the flexible optical networking paradigm: State of the art, trends, and research challenges. *Proc. IEEE* **2014**, *102*, 1317–1337. [CrossRef]
2. Gerstel, O.; Jinno, M.; Lord, A.; Yoo, S.J.B. Elastic optical networking: A new dawn for the optical layer? *IEEE Commun. Mag.* **2012**, *50*, s12–s20. [CrossRef]
3. Zhang, W.; Yue, Z.; Ye, J.; Xu, H.; Wang, Y.; Zhang, X.; Xi, L. Modulation format identification using the Calinski–Harabasz index. *Appl. Opt.* **2022**, *61*, 851–857. [CrossRef] [PubMed]
4. Jiang, X.; Hao, M.; Yan, L.; Jiang, L.; Xiong, X. Blind and low-complexity modulation format identification based on signal envelope flatness for autonomous digital coherent receivers. *Appl. Opt.* **2022**, *61*, 5991–5997. [CrossRef]
5. Huang, Z.; Zhang, Q.; Xin, X.; Yao, H.; Gao, R.; Jiang, J.; Tian, F.; Liu, B.; Wang, F.; Tian, Q.; et al. Modulation format identification based on signal constellation diagrams and support vector machine. *Photonics* **2022**, *9*, 927. [CrossRef]
6. Hao, M.; Jiang, X.; Xiong, X.; Giddings, R.; He, W. Low-complexity modulation format identification based on amplitude histogram distributions for digital coherent receivers. *Photonics* **2023**, *10*, 472. [CrossRef]
7. Mohamed, S.E.N.; Al-Makhlasawy, R.M.; Khalaf, A.A.M.; Dessouky, M.I.; Abd El-Samie, F.E. Modulation format recognition based on constellation diagrams and the Hough transform. *Appl. Opt.* **2021**, *60*, 9380–9389. [CrossRef]
8. Hao, M.; He, W.; Jiang, X.; Liang, S.; Jin, W.; Chen, L.; Tang, J. Modulation Format Identification Based on Multi-Dimensional Amplitude Features for Elastic Optical Networks. *Photonics* **2024**, *11*, 390. [CrossRef]
9. Eltaieb, R.A.; Abouelela, H.A.E.; Saif, W.S.; Ragheb, A.; Farghal, A.E.A. Modulation format identification of optical signals: An approach based on singular value decomposition of Stokes space projections. *Appl. Opt.* **2020**, *59*, 5989–6004. [CrossRef]
10. Liang, S.; Hao, M.; Xiao, R.; Jin, W. Modulation Format Identification Utilizing Polar-Coordinate-System-Based Features for Digital Coherent Receivers. *Photonics* **2025**, *12*, 190. [CrossRef]
11. Zhang, W.; Ye, J.; Yue, Z.; Xu, H.; Zhang, X. Self-evaluation clustering scheme for modulation format identification in coherent optical communication. *Opt. Fiber Technol.* **2023**, *75*, 103188. [CrossRef]
12. Guo, Z.; Liu, B.; Ren, J.; Wu, X.; Li, Y. Modulation format recognition with transfer learning assisted convolutional neural network using multiple Stokes sectional plane image in multi-core fibers. *Opt. Express* **2022**, *30*, 21990–22005. [CrossRef]
13. Do, C.; Tran, A.; Zhu, C.; Hewitt, D.; Skafidas, E. Data-aided OSNR estimation for QPSK and 16-QAM coherent optical system. *IEEE Photonics J.* **2013**, *5*, 6601609. [CrossRef]
14. Hao, M.; Yan, L.; Yi, A.; Jiang, L.; Pan, Y. OSNR monitoring using support vector ordinal regression for digital coherent receivers. *IEEE Photonics J.* **2019**, *11*, 1–11. [CrossRef]
15. Lin, X.; Octavia, A.; Ngatched, T.M.N.; Li, C. A non-data-aided OSNR estimation algorithm for coherent optical fiber communication systems employing multilevel constellations. *J. Light. Technol.* **2019**, *37*, 3815–3825. [CrossRef]
16. Xia, L.; Zhang, J.; Hu, S.; Zhu, M.; Song, Y. Transfer learning assisted deep neural network for OSNR estimation. *Opt. Express* **2019**, *27*, 19398–19406. [CrossRef]
17. Shen, F.; Zhou, J.; Huang, Z.; Li, L. Going deeper into OSNR estimation with CNN. *Photonics* **2021**, *8*, 402. [CrossRef]
18. Saif, W.S.; Maged, A.E.; Amr, M.R.; Tariq, A.A.; Saleh, A.A. Machine learning techniques for optical performance monitoring and modulation format identification: A survey. *IEEE Commun. Surv. Tutor.* **2020**, *22*, 2839–2882. [CrossRef]
19. Yu, C.; Wang, H.; Ke, C.; Liang, Z.; Cui, S. Multi-task learning convolutional neural network and optical spectrums enabled optical performance monitoring. *IEEE Photonics J.* **2022**, *14*, 1–8. [CrossRef]
20. Feng, J.; Jiang, L.; Yan, L.; Yi, A.; Pan, W. Intelligent optical performance monitoring based on intensity and differential-phase features for digital coherent receivers. *J. Light. Technol.* **2022**, *40*, 3592–3601. [CrossRef]
21. Fan, X.; Xie, Y.; Ren, F.; Zhang, Y.; Huang, X. Joint optical performance monitoring and modulation format/bit-rate identification by CNN-based multi-task learning. *IEEE Photonics J.* **2018**, *10*, 1–12. [CrossRef]
22. Cho, H.J.; Varughese, S.; Lippiatt, D.; Desalvo, R.; Tibuleac, S. Optical performance monitoring using digital coherent receivers and convolutional neural networks. *Opt. Express* **2020**, *28*, 32087–32104. [CrossRef]

23. Luo, H.; Huang, Z.; Wu, X.; Yu, C. Cost-effective multi-parameter optical performance monitoring using multi-task deep learning with adaptive ADTP and AAH. *J. Light. Technol.* **2021**, *39*, 1733–1741. [CrossRef]
24. Zhou, P.; Li, C.; Chen, D.; Zhang, Y.; Lu, Y. Cascaded modulation format identification and optical signal-to-noise ratio estimation method for optical communication system. *Opt. Eng.* **2022**, *61*, 126109. [CrossRef]
25. Wang, D.; Zhang, M.; Li, J.; Li, Z.; Li, J. Intelligent constellation diagram analyzer using convolutional neural network-based deep learning. *Opt. Express* **2017**, *25*, 17150–17166. [CrossRef]
26. Zhang, Y.; Zhou, P.; Dong, C.; Lu, Y.; Li, C. Intelligent equally weighted multi-task learning for joint OSNR monitoring and modulation format identification. *Opt. Fiber Technol.* **2022**, *71*, 102931. [CrossRef]
27. Fan, X.; Wang, L.; Ren, F.; Xie, Y.; Lu, X. Feature Fusion-Based Multi-Task ConvNet for Simultaneous Optical Performance Monitoring and Bit-Rate/Modulation Format Identification. *IEEE Access* **2019**, *7*, 126709–126719. [CrossRef]
28. Kulandaivel, S.; Jeyachitra, R.K. Combined image Hough transform based simultaneous multi-parameter optical performance monitoring for intelligent optical networks. *Opt. Fiber Technol.* **2023**, *79*, 103357. [CrossRef]
29. Lv, H.; Zhou, X.; Huo, J.; Yuan, J. Joint OSNR monitoring and modulation format identification on signal amplitude histograms using convolutional neural network. *Opt. Fiber Technol.* **2021**, *61*, 102455. [CrossRef]
30. Zhao, Y.; Yu, Z.; Wan, Z.; Hu, S.; Shu, L. Low complexity OSNR monitoring and modulation format identification based on binarized neural networks. *J. Light. Technol.* **2020**, *38*, 1314–1322. [CrossRef]
31. Wan, Z.; Yu, Z.; Shu, L.; Zhao, Y.; Zhang, H. Intelligent optical performance monitor using multi-task learning based artificial neural network. *Opt. Express* **2019**, *27*, 11281–11291. [CrossRef]
32. Xiang, Q.; Yang, Y.; Zhang, Q.; Yao, Y. Joint and accurate OSNR estimation and modulation format identification scheme using the feature-based ANN. *IEEE Photonics J.* **2019**, *11*, 1–11. [CrossRef]
33. Khan, F.N.; Shen, T.S.R.; Zhou, Y.; Lau, A.P.T.; Lu, C. Optical performance monitoring using artificial neural networks trained with empirical moments of asynchronously sampled signal amplitudes. *IEEE Photonics Technol. Lett.* **2012**, *24*, 982–984. [CrossRef]
34. Khan, F.N.; Zhong, K.; Zhou, X.; Al-Arashi, W.H.; Yu, C. Joint OSNR monitoring and modulation format identification in digital coherent receivers using deep neural networks. *Opt. Express* **2017**, *25*, 17767–17776. [CrossRef] [PubMed]
35. Yi, A.; Yan, L.; Liu, H.; Jiang, L.; Pan, Y. Modulation format identification and OSNR monitoring using density distributions in Stokes axes for digital coherent receivers. *Opt. Express* **2019**, *27*, 4471–4479. [CrossRef] [PubMed]
36. Cheng, Y.; Fu, S.; Tang, M.; Liu, D. Multi-task deep neural network (MT-DNN) enabled optical performance monitoring from directly detected PDM-QAM signals. *Opt. Express* **2019**, *27*, 19062–19074. [CrossRef]
37. Pu, Z.; Jiang, L.; Yan, L.; Yi, A.; He, H. Joint modulation format identification and OSNR monitoring based on Stokes vector distribution features for digital coherent optical receivers. *Chin. Opt. Lett.* **2024**, *22*, 050602. [CrossRef]
38. Wang, C.; Fu, S.; Wu, H.; Luo, M.; Li, X. Joint OSNR and CD monitoring in digital coherent receiver using long short-term memory neural network. *Opt. Express* **2019**, *27*, 6936–6945. [CrossRef]
39. Zhou, P.; Li, C.; Chen, D.; Zhang, Y.; Lu, Y. Joint Modulation Format Identification and Optical Signal-to-Noise Ratio Monitoring Based on Ternary Neural Networks. *IEEE Access* **2022**, *10*, 133324–133332. [CrossRef]
40. Yang, F.; Bai, C.; Chi, X.; Zhang, R.; Qi, Q. Intelligent joint multi-parameter optical performance monitoring scheme based on HT images and MT-ResNet for elastic optical network. *Opt. Fiber Technol.* **2024**, *82*, 103599. [CrossRef]
41. Li, J.; Xiong, W.; Wang, P.; Chen, Y.; Liu, J. Optical signal monitoring using multi-task residual network. *Optik* **2022**, *259*, 169003. [CrossRef]
42. Zhou, T.; Xu, H.; Bai, C.; Yang, L.; Sun, W. Simultaneous baud rate/modulation format identification and multi-parameter optical performance monitoring using multi-task learning with enhanced picture of Radon transform. *Opt. Fiber Technol.* **2022**, *70*, 102873. [CrossRef]
43. Cheng, Y.; Zhang, W.; Fu, S.; Tang, M.; Liu, D. Transfer learning simplified multi-task deep neural network for PDM-64QAM optical performance monitoring. *Opt. Express* **2020**, *28*, 7607–7617. [CrossRef] [PubMed]
44. Sindhumitha, K.; Jeyachitra, R.K.; Manochandar, S. Joint modulation format recognition and optical performance monitoring for efficient fiber-optic communication links using ensemble deep transfer learning. *Opt. Eng.* **2022**, *61*, 116103. [CrossRef]
45. Zhang, J.; Li, Y.; Hu, S.; Zhang, W.; Wan, Z. Joint modulation format identification and OSNR monitoring using cascaded neural network with transfer learning. *IEEE Photonics J.* **2021**, *13*, 1–10. [CrossRef]
46. Chai, J.; Chen, X.; Zhao, Y.; Yang, T.; Wang, D. Joint symbol rate-modulation format identification and OSNR estimation using random forest based ensemble learning for intermediate nodes. *IEEE Photonics J.* **2021**, *13*, 1–6. [CrossRef]
47. Zhao, Q.; Zhang, Q.; Xin, X.; Yao, H.; Gao, R. Neural network-assisted joint MFI and OSNR monitoring based on multi-model fitting. *Opt. Express* **2025**, *33*, 41194–41209. [CrossRef] [PubMed]
48. Li, J.; Ma, J.; Liu, J.; Lu, J.; Zeng, X. Modulation format identification and OSNR monitoring based on multi-feature fusion network. *Photonics* **2023**, *10*, 373. [CrossRef]
49. Liang, J.; Bao, Y. A modulation format recognition and optical signal-to-noise ratio monitoring scheme based on residual network and Taylor score pruning. *PLoS ONE* **2025**, *20*, e0333936. [CrossRef]

50. Zeng, Q.; Lu, Y.; Liu, Z.; Zhang, Y.; Li, H. Multi-task metric learning for optical performance monitoring. *Opt. Fiber Technol.* **2024**, *87*, 103927. [CrossRef]
51. Zhang, Y.; Zhou, P.; Liu, Y.; Wang, J.; Li, C. Fast adaptation of multi-task meta-learning for optical performance monitoring. *Opt. Express* **2023**, *31*, 23183–23197. [CrossRef] [PubMed]
52. Zeng, Q.; Kong, Y.; Zhou, P.; Lu, Y. Adaptive multi-task convolutional neural network for optical performance monitoring. *Opt. Commun.* **2025**, *583*, 131702. [CrossRef]
53. Huang, G.; Liu, Z.; Van Der Maaten, L.; Weinberger, K.Q. Densely connected convolutional networks. In Proceedings of the IEEE Conference on Computer Vision and Pattern Recognition (CVPR), Las Vegas, NV, USA, 27–30 June 2017.
54. He, K.; Zhang, X.; Ren, S.; Sun, J. Deep residual learning for image recognition. In Proceedings of the IEEE Conference on Computer Vision and Pattern Recognition (CVPR), Las Vegas, NV, USA, 27 June–1 July 2016.
55. Sandler, M.; Howard, A.; Zhu, M.; Zhmoginov, A.; Chen, L.-C. MobileNetV2: Inverted residuals and linear bottlenecks. In Proceedings of the IEEE Conference on Computer Vision and Pattern Recognition (CVPR), Salt Lake City, UT, USA, 18–22 June 2018.
56. Simonyan, K.; Zisserman, A. Very deep convolutional networks for large-scale image recognition. In Proceedings of the International Conference on Learning Representations (ICLR), San Diego, CA, USA, 7–9 May 2015.

Disclaimer/Publisher's Note: The statements, opinions and data contained in all publications are solely those of the individual author(s) and contributor(s) and not of MDPI and/or the editor(s). MDPI and/or the editor(s) disclaim responsibility for any injury to people or property resulting from any ideas, methods, instructions or products referred to in the content.